Applied Materials Today 34 (2023) 101881

Contents lists available at ScienceDirect

Applied Materials Today

journal homepage: www.elsevier.com/locate/apmt

Hematene: A sustainable 2D conductive platform for visible-light-driven photocatalytic ammonia decomposition

Jana Dzíbelová [a,b,1], S.M. Hossein Hejazi [a,c,1], Veronika Šedajová [a], David Panáček [a], Petr Jakubec [a,*], Zdeněk Baďura [a,b], Ondřej Malina [a], Josef Kašlík [a], Jan Filip [a], Štěpán Kment [a,c], Michal Otyepka [a,d,*], Radek Zbořil [a,c,*]

[a] Regional Centre of Advanced Technologies and Materials, Czech Advanced Technology and Research Institute (CATRIN), Palacký University Olomouc, Šlechtitelů 241/27, Olomouc 779 00, Czech Republic
[b] Department of Experimental Physics, Faculty of Science, Palacký University Olomouc, 17. listopadu 1192/12, Olomouc 779 00, Czech Republic
[c] Nanotechnology Centre, Centre of Energy and Environmental Technologies, VŠB–Technical University of Ostrava, 17. listopadu 2172/15, Poruba, Ostrava 708 00, Czech Republic
[d] IT4Innovations, VŠB–Technical University of Ostrava, 17. listopadu 2172/15-Poruba, Ostrava 708 00, Czech Republic

ARTICLE INFO

Keywords:
Hematene
Ammonia
Hydrogen Production
Photocatalytic decomposition

ABSTRACT

The emerging class of 2D non-van der Waals (n-vdW) materials, including 2D iron oxides, possesses unique properties and high applicability, making them attractive for various technological applications. However, the synthesis of these materials through a scalable and eco-friendly method remains a challenge, as most known chemical exfoliation processes require toxic organic solvents. In this study, we report a green synthesis of 2D hematene (α-Fe_2O_3) using an ultrasound-supported exfoliation method of earth-abundant iron oxide ore in a pure aqueous solution. The resulting hematene sheets, only a few nanometers thick, exhibit superior electrochemical performance in terms of charge transfer processes, making them ideal for photocatalytic applications. By doping a conductive hematene substrate with ruthenium, we demonstrate a synergistic effect for generating electrons and holes under visible light irradiation. Using this approach, we successfully decomposed ammonia into hydrogen and nitrogen, highlighting the potential of this novel class of environmentally-friendly photocatalysts for clean energy production. Overall, our water-assisted scalable synthesis of hematene offers a promising strategy for producing efficient and sustainable photocatalysts.

1. Introduction

The discovery of two-dimensional (2D) materials has kindled immense interest among scientists as they exhibit unique chemical, physical, and electronic properties, compared to their 3D counterparts [1]. Their properties can be exploited in various applications, including electronics [2,3], sensors [4–6], energy storage [7–9], and spintronics [10,11]. Owing to their bonding nature, 2D materials can be sorted into two main classes: i) van-der Waals (vdW) 2D materials, such as graphene, black phosphorus (BP), transition metal dichalcogenides, metal-organic frameworks (MOFs), or MXenes, where the strong chemical bonding is located in-plane and the weak vdW bonding out-of-plane; and ii) non-van-der Waals (n-vdW) 2D materials like metal chalcogenides, oxides, nitrides, and phosphides, which exhibit strong chemical bonding in all three directions [12]. The n-vdW materials have a layered structure with an overall thickness of around 10 nm and encompass high energy surfaces [13].

Methodologies used for the synthesis of n-vdW materials include a self-assembly approach [14–16], exfoliation [17], lamellar intermediate exfoliation [18,19], and topochemical transformation [12,20,21]. The exfoliation process has been adopted as the most convenient strategy for the preparation of iron oxide derived n-vdW 2D materials such as hematene (2D α-Fe_2O_3), magnetene (2D Fe_3O_4), ilmenene (2D $FeTiO_3$), and chromiteen (2D $FeCr_2O_4$) [22]. All these materials were prepared from natural ores in organic solvents (typically DMF; N, N-dimethylformamide), deploying ultrasonication, with that being the

* Corresponding authors at: Regional Centre of Advanced Technologies and Materials, Czech Advanced Technology and Research Institute (CATRIN), Palacký University Olomouc, Šlechtitelů 241/27, Olomouc 779 00, Czech Republic.
E-mail addresses: p.jakubec@upol.cz (P. Jakubec), michal.otyepka@upol.cz (M. Otyepka), radek.zboril@upol.cz (R. Zbořil).
[1] These authors contributed equally.

https://doi.org/10.1016/j.apmt.2023.101881
Received 31 March 2023; Received in revised form 30 June 2023; Accepted 13 July 2023
Available online 29 July 2023

main drawback of these exfoliation processes due to the inherent toxicity of DMF and unwanted surface functionalization [23]. Because of the DMF toxicity [24,25], the European Union is adopting regulations restricting its use from December 2023 onwards [26]; hence the need for the development of alternative exfoliation processes in nontoxic solvents.

Since the amount of fossil fuels is limited, alongside the fact that global energy consumption is estimated to increase at least twice by the midcentury compared to the present time [27], the exploitation of renewable and sustainable energy sources represents one of the most important tasks. Previously published reports show that n-vdW materials such as hematene (2D α-Fe_2O_3), magnetene (2D Fe_3O_4), ilmenene (2D $FeTiO_3$), and chromiteen (2D $FeCr_2O_4$) have strong potential in the field of photoelectrochemistry, where the combination of these allotropes with Ti nanotubes shows excellent results [28,29]. N-vdW materials also hold great potential in various electrocatalytic applications targeting the energy conversion processes, including water splitting (HER and OER reactions), CO_2 reduction reaction (CRR), nitrogen reduction and oxidation reactions (NRR and NOR), NO_x reduction and NH_3 oxidation [12]. Up to now, the highest electrocatalytic activity is achieved with noble metals, which represents the main drawback for the scalable application of these electrocatalysts on the commercial level, mainly due to their price and availability. Thus, the development of novel materials with enhanced electrocatalytic and/or photocatalytic activity towards sustainable energy conversion is highly desired.

An ammonia decomposition reaction is a promising alternative to fossil fuels that leads to the release of hydrogen and nitrogen, thus overcoming the challenges of hydrogen storage [30,31]. Ammonia is an ideal hydrogen carrier since it has a high gravimetric (17.8 wt. % H_2) and volumetric (121 kg H_2 m^{-3} in the liquid form) H_2 density and produces a high amount of CO_x free hydrogen after decomposition [30, 32]. Therefore, a clean process based on renewable energy sources to convert NH_3 to H_2 (as a fuel) and N_2 (as a harmless gas) is an important scientific challenge. The aqueous ammonia decomposition (1) is an uphill reaction and the required reaction energy can be provided by the sun light photons using photocatalyst materials [33].

$$NH_3(aq.) \rightarrow 3/2H_2(g) + 1/2N_2(g) \quad (1)$$

$$\Delta G_{298K} = 27 \text{ kJ mol}^{-1}$$

Currently, only a few photoactive materials are found to be able to decompose the aqueous ammonia solution, including TiO_2 [34–38], ZnO [39,40], ZnS [33], C_3N_4 [41], graphene, and other carbon based materials [42]. However, all these materials suffer from several drawbacks limiting their wide application in practice. TiO_2 is a very popular photoactive material that has relatively low cost, high chemical stability, and good light conversion efficiency. However, the efficiency is still relatively low because of the fast recombination of the photoinduced charge transfer. Another handicap is that TiO_2, for instance, works only under the UV illumination [34,39,40]. The complicated multiple-step synthesis of the photocatalysts using various toxic solvents (e.g., DMF) [40,42] limits the practical applicability of other photocatalysts. Therefore, the preparation of photocatalysts by green chemistry principles while relying on cheap and eco-friendly transition metal oxides as successful N_2 activators remains one of the major challenges in the field of photocatalytic decomposition of ammonia.

In this work, we show that the two-dimensional hematene can be synthesized by a green environmentally friendly scalable method from an earth abundant raw material—iron oxide ore specularite. The hematene sheets were a few nanometers in thickness and gave a satisfactory electrochemical performance in terms of the charge transfer limiting processes. Reflecting these properties, we exploited the combination of a conductive 2D hematene substrate with the catalytic surface of RuO_2 nanoparticles to test them as a photocatalytical platform suitable for the production of hydrogen under the visible light irradiation. The obtained results clearly proved that this nanocomposite exhibited a synergic effect in terms of the generation of electrons and holes. In this case, the holes oxidized the already absorbed ammonia through the quasi-metallic ruthenium oxide and left the electrons in hematene for the reduction of ammonia under the visible light irradiation. The excellent photocatalytic performance of the ruthenium oxide-loaded hematene supported by the fact that the entire photocatalyst can be prepared by environmentally friendly and scalable ways indicates that the developed strategy is viable for the fabrication of a novel class of photocatalysts suitable for the production of hydrogen.

2. Experimental

2.1. Common reagents

Potassium ferricyanide (p.a.) was purchased from Lachema (Brno, Czech Republic) and potassium chloride (p.a.) was obtained from Penta. Iron oxide ore specularite was obtained from the Moravian Museum (Brno, Czech Republic). The $RuCl_3.xH_2O$ (content of Ru: 38% min) and ammonium hydroxide (28 % NH_3) were purchased from Alfa Aesar. The magnesium oxide powder was purchased from Sigma Aldrich. Deionized water (DI) was used for the preparation of all aqueous solutions and dispersions.

2.2. Synthesis of hematene and loading with ruthenium

The hematite ore specularite was ground into a fine powder using a Retsch Planetary Ball Mill PM 100. The bulk sample was ball milled for 5 minutes, allowed to cool down to avoid excessive heating that might have led to undesirable effects, e.g., sintering, and then ball milled again for another 5 minutes. The ensued fine hematite powder (2 g) was dispersed in 180 mL of DI water, mixed thoroughly with a vertical rotator (Heidolph) at 45 rpm for 96 h, and sonicated in a bath sonicator (Branson; power output: 130 W, frequency: 40 kHz) for 48 h. The exfoliated hematene sheets were separated by sedimentation from the unexfoliated specularite and further processed to the desired concentration using centrifugation (centrifuge Sigma 4–16 K, Sigma Laborzentrifugen GmbH, Osterode am Harz, Germany) at 21 000 rcf. The unexfoliated powder of hematite was collected and used again for the preparation of hematene sheets.

The ruthenium loading was done via the impregnation method. First, the hematene powders were separated from the solution by centrifugation and dried at 80 °C for 1 h. After preparing the predefined concentration of $RuCl_3$ in DI water, the measured amount of dried hematene was added to the solution and stirred for 3 hours. Then the emulsion was centrifuged to separate the solid precipices from the supernatant. The centrifugation was repeated twice while it was washed with DI water to remove the extra amount of $RuCl_3$. Then, the powders were dried at 80 °C for 1 h and calcined at 300 °C for 3 h in air atmosphere.

2.3. Microscopic techniques

Scanning electron microscopy (SEM) and atomic force microscopy (AFM) analyses were performed with a FIB-SEM instrument SCIOS 2 (Thermo Fisher) equipped with an integrated AFM Litescope (NenoVision). The sample was analyzed on a Si wafer. The correlative probe and electron microscopy (CPEM) was used for the surface analysis, allowing simultaneous SEM and AFM data acquisition at the same place in the same coordinate system. For SEM imaging, an accelerating voltage of 2 kV, a beam current of 25 pA, and an ETD detector was deployed. The self-sensing Akiyama probe in the tapping mode was used for the AFM measurement. High-resolution TEM (HRTEM) images including STEM-HAADF (high-angle annular dark-field imaging) analyses for elemental mapping of the products were collected with an FEI Titan HRTEM microscope using an operating voltage of 80 kV. For these analyses, a droplet of dispersion of the material in ultrapure H_2O at a concentration of ~0.1 mg mL^{-1} was deposited onto a carbon-coated copper grid and

dried.

2.4. Spectroscopic measurements

The X-ray photoelectron spectroscopy (XPS) measurements were carried out by a PHI VersaProbe II probe (Physical Electronics) with an Al Ka source (15 kV, 50 W). The measured spectra were deconvoluted using the MultiPak software (Ulvac-PHI, Inc.). The Raman spectra for all the samples were recorded on a DXR Raman microscope using a diode laser with an excitation line of 633 nm. The EPR spectra were collected on a X-band (~9.14–9.17 GHz) spectrometer JEOL JES-X-320 equipped with a variable He temperature set-up ES-CT470 apparatus. The experimental temperature was set to 80 K. The quality factor (Q) was kept above 6000 for all measurements to make the spectra comparable. High purity quartz tubes (Suprasil, Wilmad, ≤0.5 OD) were used as a sample holder. The accuracy of the *g*-values was determined by comparing them with a Mn^{2+}/MgO standard (JEOL standard). The microwave power was set to 1.0 mW to avoid any power saturation effects. A modulation width of 1 mT and a modulation frequency of 100 kHz were used. All the EPR spectra were collected with a time constant of 30 ms and a sweep time of 4 min.

2.5. Structural and phase analysis

X-ray diffraction (XRD) patterns of bulk iron ore and exfoliated hematene samples were collected on a PANalytical X'Pert PRO diffractometer (iron-filtered Co Kα radiation: λ = 0.178901 nm, 40 kV and 30 mA) in a Bragg-Brentano geometry equipped with an X'Celerator detector, programmable divergence, and diffraction beam anti-scattering slits. Each sample was placed on a zero-background Si slide, gently pressed, and scanned in the 2θ range from 5° to 105° The phase identification was performed using PANalytical HighScore Plus software with PDF-4+ and ICSD databases.

2.6. Electrochemical measurements

All the electrochemical measurements in a three-electrode set-up were performed at ambient room temperature (22 ± 2 °C) using the Metrohm Autolab PGSTAT128N potentiostat (MetrohmAutolab B.V., Netherlands). The obtained electrochemical data sets were evaluated by the NOVA software package (version 1.11.2). The system comprised a glassy carbon electrode (GCE) serving as the working electrode, a platinum wire electrode used as the counter electrode and an Ag/AgCl (3 M KCl) electrode as the reference electrode. The GCE was modified as follows: a 10 μL drop of a sample dispersion in DI water (concentration of ≈ 1 mg mL^{-1}) was coated onto the surface of the GCE electrode and allowed to dry at ambient temperature to form a thin film. Potassium chloride (c = 1 mol L^{-1}) containing potassium ferricyanide (c = 5 mmol L^{-1}) as a redox probe served as a supporting electrolyte for impedance measurements. Individual settings for impedance spectroscopy measurements (EIS) are given in the Figure legends.

2.7. Photocatalyst characterization and photodecomposition of ammonia

The ultraviolet-visible diffuse reflectance spectra (UV–Vis DRS) of the synthesized samples were obtained by a Specord 250 plus (Analytik Jena, Jena, Germany) spectrophotometer. An integrating sphere was used to collect the spectrum. The magnesium oxide powder served as a background reference sample.

The photodecomposition of NH_3 was conducted in a 17.5 mL quartz reactor. After sono-dispersion of the photocatalyst in 10 mL of ammonium hydroxide, the rector was tightly sealed with a rubber septum. Since dissolved oxygen in a solution could act as an electron scavenger, it was bubbled with argon for 15 min to remove the oxygen. Then, the sample was illuminated under LED (Solis® High-Power LED from Thorlabs) with the power of 3 W·m^{-2} and a wavelength of 400–700 nm.

To avoid the thermal decomposition of ammonia, the reaction was conducted in a water bath to keep the temperature of the solution at 24 °C during the reaction. The photocatalytically evolved hydrogen was detected with a gas chromatograph GCMS-QP2010 SE (Shimadzu, Kyoto, Japan) and a TCD (Thermal conductivity detector) using Ar as carrier gas.

3. Results and discussion

3.1. Structural, morphological, and (electro)chemical characterization of hematene

Multi-layered hematene sheets were prepared via an exfoliation process from an (ultra)pure water dispersion of specularite, as discussed earlier in the experimental section. The morphology of the hematene sample was evaluated by a CPEM technique (combination of SEM and AFM analysis) and a HRTEM analysis, as shown in Fig. 1a–f and Fig. S1a–c. It is evident that the exfoliated sample was of a 2D-like nature with the lateral sizes in units of micrometers (Fig. 1a–c). Homogenous distribution of the individual elements such as iron or oxygen (Fig. S1b) implied high purity of the prepared hematene sample, which was affirmed by an EDAX analysis (Fig. S1c), ultimately confirming the dominant presence of these elements; the appearance of the copper element related to the grid used for the HRTEM analysis. The AFM analysis (Fig. 1b,c) and the related height profile (Fig. 1d) revealed that the thickness of the representative sheet was of around 5 nm. The thickness of the molecular dynamic simulated hematene (001) and (010) planes was estimated as 3.98 Å and 3.2 Å, respectively, corroborating a previously published report [28]. Thus, the thickness of 5 nm represented ≈ 12 hematene layers in the final product. A higher number of layers validates the theory that the selection of a chemical solvent decidedly affects the possibility of exfoliating the sample by ultrasonic irradiation up to individual layers [43]. As expected, the sonochemical preparation strategy of hematene from (ultra)pure water did not enable to provide a mono or two-layered system. To prove the size and thickness of the hematene material, CPEM images with related height profiles were collected from different sheets, and are depicted in Fig. S2. The 2D structure of the hematene sample was also confirmed from magnetic data measurements. Details of those experiments and related discussion are provided in the ESI. The composition of the product was also supported by XPS, as shown in the box (Fig. 1e,f). The obtained HR-XPS spectrum of the Fe 2p region (Fig. 1e) revealed two peaks at around 712 and 725 eV, corresponding to Fe $2p_{3/2}$ and Fe $2p_{1/2}$, respectively [28,44]. The satellite peak located at around 719 eV further indicated the Fe^{3+} oxidation state [44]. As evident from the deconvolution, both spin-orbit components were fitted with two peaks. These fitted peaks served more as a reference, indicating a trend based on already published studies [45,46]; the transition metals in their 2p states should be fitted by multiple components, representing the multiplet splitting. The HR-XPS spectrum of the O 1 s region (Fig. 1f) was fitted in three components, based on previous reports [47,48], corresponding to the lattice incorporated oxygen at higher binding energies and the surface present oxygen (in a defect state and as surface oxidation [28,47,48]) at lower binding energies, respectively.

The nature of the hematene sample was also evaluated by means of Raman spectroscopy. Fig. 2a shows the Raman spectra of original specularite ore in comparison with the hematene sample. The positions of the most important bands were found at around 224 and 495 cm^{-1} (A_{1g} modes) and 249, 290, 409, 611 cm^{-1} (E_g modes). The broad intense band visible at around 1318 cm^{-1} was connected with the scattering of two magnons in the structure of the hematite ore [49]. As expected, the hematene showed the position of the most important bands, similarly to specularite. Nevertheless, the additional band was observed at 663 cm^{-1}, which can be assigned to the structural disorders inside the crystal lattice (E_u modes) related to the 2D crystal structure [28,48,50,51]. The crystalline structure and chemical phase purity of both the original

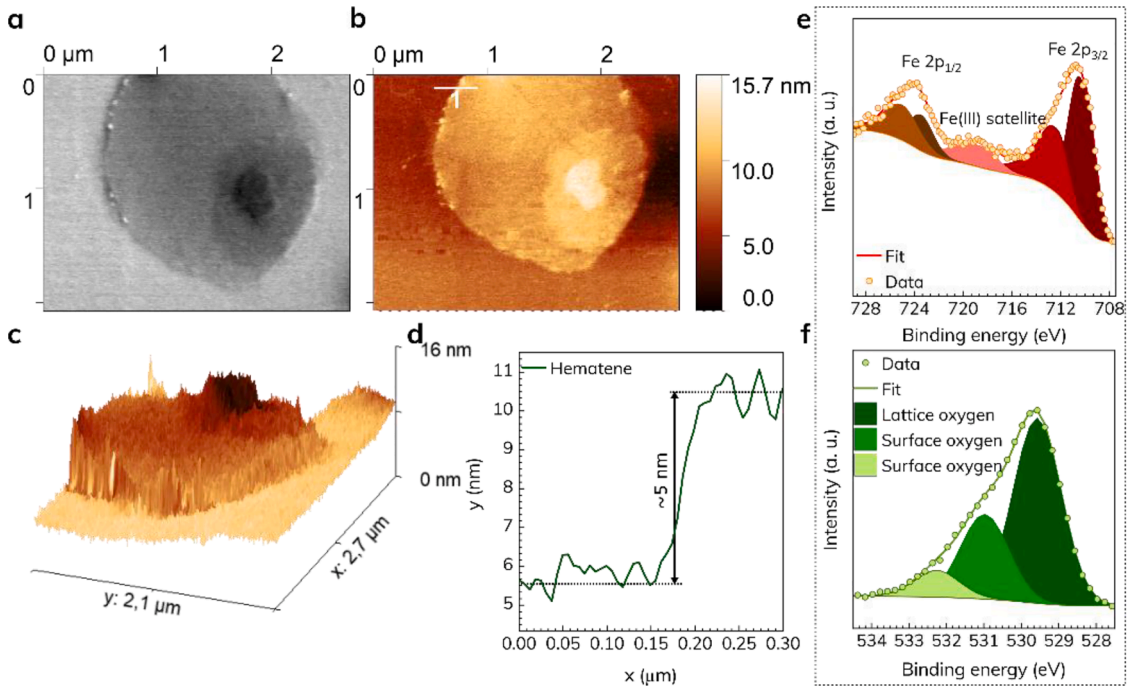

Fig. 1. (a–c) CPEM images of hematene sheet and related height profile (d); (e) HR-XPS spectrum of Fe 2p and (f) O 1 s region.

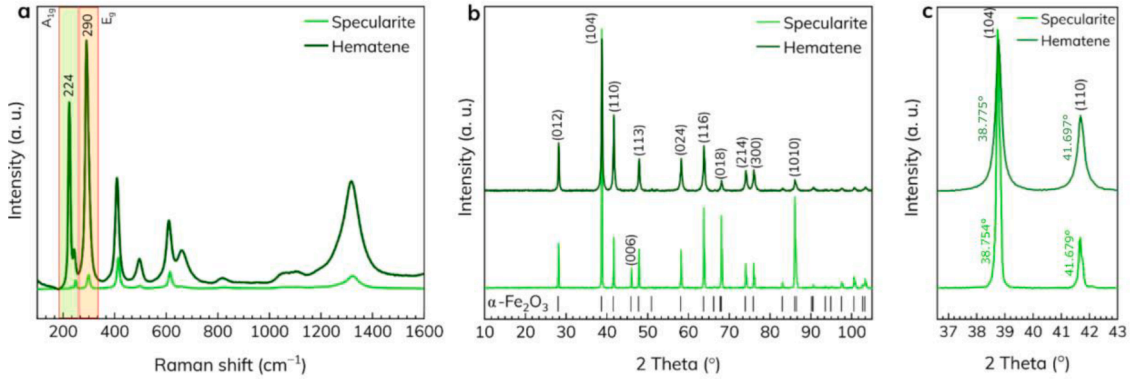

Fig. 2. (a) Raman spectra of specularite and hematene; (b) XRD patterns of specularite and hematene; (c) detail of XRD patterns showing the broadening and shift of hematene diffraction peaks compared to parent specularite.

specularite and the exfoliated hematene were additionally evaluated by XRD measurements (Fig. 2b). The collected patterns illustrate that both samples contained only the α-Fe_2O_3 phase of the corundum crystal structure (JCPDS card 01–089–0599, rhombohedral structure, space group R-3c), which rules out the presence of any other crystalline phases. The diffraction pattern of hematene (lattice parameters: a = 5.035 Å and c = 13.745 Å) showed that the diffraction peaks were slightly broadened and slightly shifted in their position, compared to the original specularite (lattice parameters: a = 5.034 Å and c = 13.742 Å). These effects are visible in Fig. 2c, providing a detail about the positions of the two diffraction peaks, where the diffraction on the (104) plane is typically dominant for the α-Fe_2O_3 structure. Such observation is consistent with the exfoliation of hematite in previous studies [28,52], where the broadening of the lines is related to the reduction in crystallite size [17, 53].

Prior to the modification of the hematene with ruthenium, the electrochemical performance of specularite and its 2D analogue was evaluated by means of impedance spectroscopy (EIS). Fig. 3a illustrates the EIS spectra as the Nyquist plot of a bare glassy carbon electrode (GCE) and GCE modified with the specularite precursor and the hematene sample. As visible in Fig. 3b, all EIS spectra should be fitted with a simple Randles circuit, which illustrates the non-complicated electrochemical behavior of all the tested materials. In general, resistance R_S located at point A (see Fig. 3b) was assigned to the solution resistance or the so-called ESR resistance (known also as the internal resistance), whereas the diameter of the semicircle $R_{AB} = R_B - R_A$ represented the sum of the electrode and contact resistance and the charge transfer resistance (R_{ct}) [54,55]. A magnified version of the Nyquist plot (inset of Fig. 3a) revealed that the charge transfer resistance (R_{ct}) increased significantly when the working electrode (R_{ct} = 40.4 Ω) was modified either with the specularite (R_{ct} = 222 Ω) or the hematene (R_{ct} = 173 Ω). Such behavior suggested the successful immobilization of both materials on the surface of the working electrode. It is perfectly clear that the diameter of the semicircle was smaller in favor of the hematene (inset of Fig. 3a), which reflected a better contact of the hematene film with the surface of the working electrode and thus a lower impact on the charge transfer limiting processes. Therefore, it can be expected that the electron transfer was enhanced in that case.

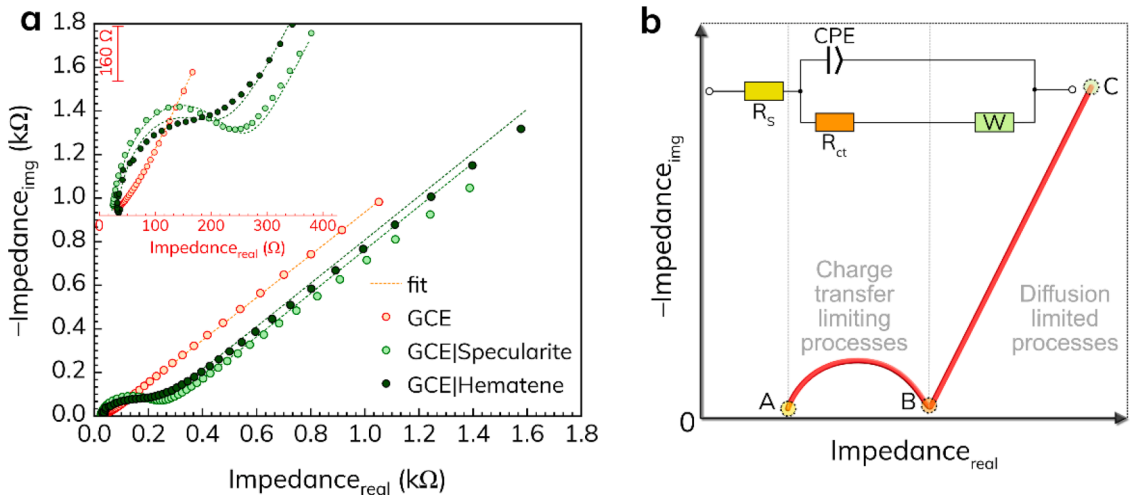

Fig. 3. (a) Nyquist plot of bare GCE and GCE modified with specularite and hematene; parameters of EIS: frequency range from 100 kHz to 0.1 Hz, the amplitude of 10 mV and half-wave potential of 0.24 V; (b) visualization of Nyquist plot and related equivalent circuit used for the data evaluation.

3.2. Photocatalyst characterization

Fig. 4 shows the HRTEM images of the hematene and the Ru-hematene together with the elemental analysis. The dominant crystal plane distance in the hematene was 2.7 Å, which was related to the (104) plane, while the presence of ruthenium oxide was confirmed by its dominant crystal plane distance 3.2 Å related to the (110) plane. Both structures in Ru-hematene were also identified by XRD (Fig. S6).

The EDS elemental analysis of the Ru-hematene showed a well dispersed ruthenium oxide particles without any sign of agglomeration at the surface of the hematene structure as catalyst sites for ammonia oxidation. This uniform dispersion of ruthenium oxide helped to increase the charge separation and therefore its photoactivity.

The XPS technique was employed to determine the oxidation states of the ruthenium in the Ru-hematene sample. As shown in Fig. 5a, the HR-XPS Ru 3d region was analyzed and deconvoluted to reveal two oxidation states of ruthenium. The Ru^{4+} peak at around 280.5 eV further proved the presence of RuO_2 species [56–58], which was in agreement with the EPR observations (Fig. 5d), and was reasonable to expect due to the heat treatment of the sample at 300 °C. The adjacent Ru^{3+} band below 282 eV indicated the existence of the Ru(III) [56,57,59] atoms, which can be further explained by the co-presence of the chlorine in this sample (1.2 at.% coming from the precursor) (Fig. S5). The carbon content (C 1 s peak) is intrinsic to the hematene itself and was not fully eliminated during the heating process. These XPS observations confirmed the previous characterization techniques as well as the photocatalytic activity [58–62]. Fig. 5b shows the valence band XPS (VB-XPS) of the hematene and the Ru-hematene. The position of the valence band edge of the hematene did not change after loading with ruthenium (+1.1 eV), while the density of states (DOS) showed an increase at around +0.5 eV below the Fermi level within the band gap. This tail was possibly due to the presence of the RuO_2 species, creating heterojunction at the surface of hematene, which provided a mid-band gap energy state levels around +0.5 eV below the hematene Fermi level (Fig. 5c). These energy state levels were able to facilitate the photogenerated hole transportation from the hematene to RuO_2 and oxidize ammonia to N_2 by providing orbital overlaps [63]. On the other hand, the photogenerated electrons went through the hematene and reduced the ammonia to hydrogen (Fig. 5c). This spatial charge separation in the place of RuO_2 and the hematene heterojunction resulted in higher photoactivity of this photocatalyst in comparison with the bare hematene.

To obtain more detailed information about the structure and the nature of the Ru coupling mechanism on hematene, we carried out an electron paramagnetic resonance (EPR) study at low temperature (T = 80 K). In a neat hematene, in spite of assuming the presence of a large number of spin-containing defects located on the edges of individual flakes, the recorded spectrum in a frozen water matrix was indeed EPR

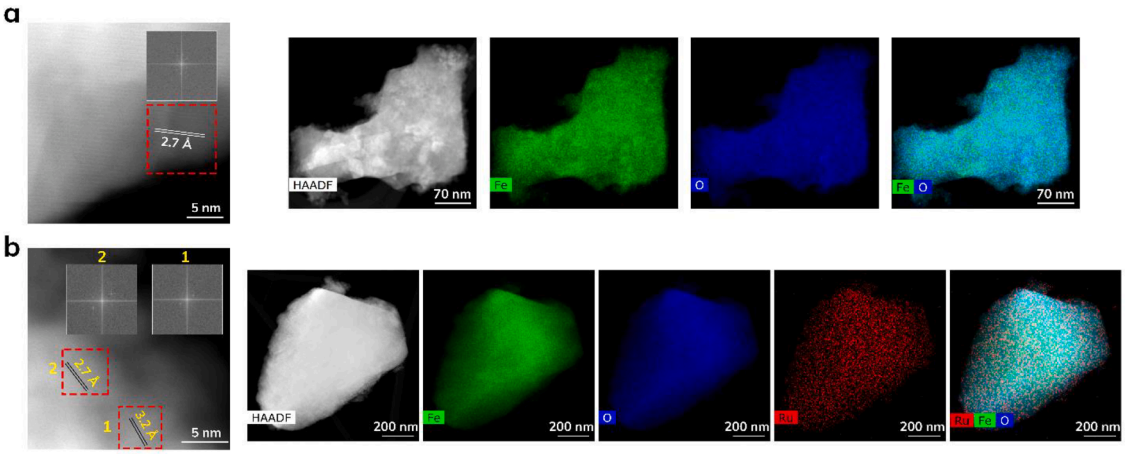

Fig. 4. HRTEM image (left), STEM-HAADF images and elemental EDS mapping (right) of (a) hematene and (b) Ru-hematene. The insets show the FFT patterns of the shown area by dashed red rectangle.

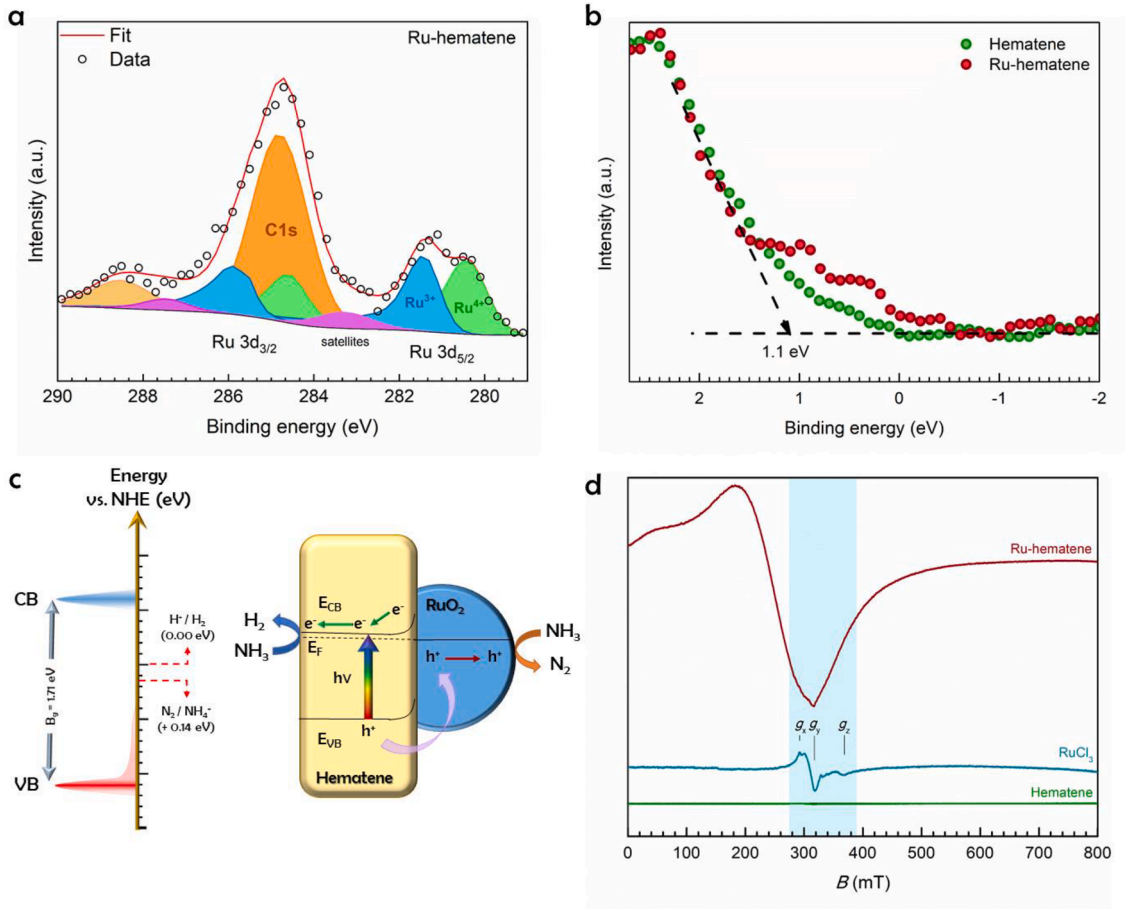

Fig. 5. (a) Deconvolution of HR-XPS of Ru 3d orbital of Ru-hematene photocatalyst; (b) Valence band XPS (VB-XPS) of hematene and Ru-hematene; (c) Schematic density of states (DOS) and band edge positions of the main electronic levels of Ru-hematene relative to the energy levels of the redox couples of aqueous ammonia (left) and the proposed mechanism of ammonia photodecomposition by Ru-hematene photocatalyst (right). (d) X-band CW EPR spectra of neat hematene (green line), $RuCl_3$ (blue spectrum) and EPR envelope of hematene decorated by RuO_2 nanoparticles (red curve), dispersed in DI H_2O and recorded in the frozen solution (T = 80 K).

silent (green line in Fig. 5d). Since, this material exhibited antiferromagnetic ordering at T below 250 K, this phenomenon was not unexpected. Nevertheless, a statistical percentage of an effective spin moment ($d\chi^{II}/dB \neq 0$) should be left at 80 K, which raises a question why these effective spins cannot be observed at X-band frequency. The reasoning can be back traced in the fast spin-lattice relaxation of the Fe^{3+} centers under an exchange coupled regime, and in the large zero-field splitting term arising from the coupling scheme, which renders the system to be more likely a non-Kramer multiplet.

The resulting EPR spectrum of $RuCl_3$ as the metal-salt source for the decoration of the hematene flakes is shown for comparison in Fig. 5d (blue line). The rhombic resonant line of Ru cations in +3 oxidation state showed small g-tensor anisotropy, with components at $g_x = 2.220$, $g_y = 2.094$ and $g_z = 1.802$. These g-values are typical for Ru^{3+} ions, however, here, they were slightly smaller than in the Ru^{3+} complexes coordinated to the organic frameworks [64] because of the absence of a strong ligand field. In Fig. 5d (red spectrum), the EPR envelope of Ru-hematene showed significant differences compared with the EPR spectra of the two previous reference samples. In the EPR spectrum of the composite Ru-hematene material, a very broad and asymmetric resonant line became dominant. This line exhibited an average g-value of about ~ 2.7, which was fully consistent with clustered Fe^{3+} cations on the layered surface that became perturbed by the Ru cations in a way that their antiferromagnetically coupling interaction, as seen in the neat hematene, was strongly weakened and therefore EPR detectable. We assume that the Ru ions reacted with oxygen on the top of the hematene surface to form small RuO_2 nanoparticles, and by doing so, they partially altered the fraction of the Fe-O-Fe superexchange path. Therefore, the observed effect on the resonance spectrum, combined with clear asymmetry in the broad resonance, suggests this was a surface localization of these defects, which is in full agreement with the 2D structure of the hematene flakes and the TEM analysis (Fig. S1a). Furthermore, in the area highlighted in blue in the EPR spectrum of the Ru-hematene (Fig. 5d), a weak modulation of an Fe^{3+} envelope around 310 mT was observed. It was positioned at $g \sim 2.09$, a value that is in line with the signal of Ru^{3+}, and probably located on the surface of the RuO_2 nanoparticles, as usually observed [65]. Since the Ru loading was very low, and we could detect only the Ru^{3+} species via EPR, the signal of Ru was observed as weak modulation in the broad resonant line of Fe^{3+}. However, part of the Ru^{3+} fragments in the EPR spectrum can also be an indicator of a small amount of residual $RuCl_3$ salt in the resulting material, which was also observed in XPS.

3.3. *Photocatalytic decomposition of HN_3 via ruthenium loaded hematene*

Prior to photocatalytical experiments, both pristine and Ru-hematene were evaluated by means of UV–VIS spectroscopy to assess the suitability of both materials for photodecomposition of ammonia. The band edge absorption for both samples was around 729 nm, as shown in Fig. 6a. Therefore, these materials can absorb both UV and a visible part of the light spectrum. The reason for the dark red color in the samples is also related to this wide absorption region. The amount of

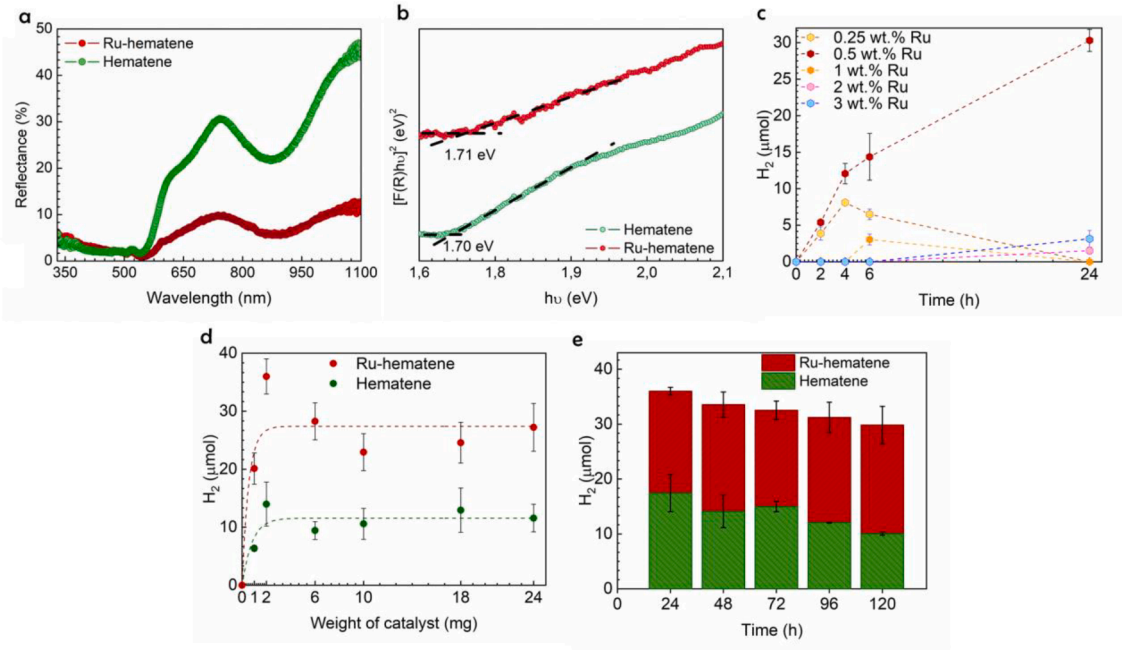

Fig. 6. (a) UV–VIS DRS of hematene and Ru-hematene and (b) corresponding Tauc plot based on Kubelka-Munk model to calculate the optical band gap of hematene and Ru-hematene; (c) Optimizing the loading amount of Ru co-catalyst for H_2 evolution of ammonia photodecomposition. The reactors were loaded with 8 mg of photocatalyst; (d) The amount of evolved H_2 from photodecomposition of ammonia with different loading amount of pristine hematene and Ru-hematene. The reactors were under illumination for 24 hours; (e) Reusability of 2 mg of hematene and Ru-hematene for H_2 evolution from ammonia photo decomposition. After each cycle, the solution was sonicated and bubbled with Ar for 15 min. In all cases, the reactor was under visible LED illumination (wavelength from 400 to 700 nm, power 3 $W{\cdot}m^{-2}$).

light absorption (especially in the visible region) was highly increased after adding ruthenium. This huge increase in visible light absorption fulfills one of the main conditions of an ideal photocatalyst for photocatalytic reactions. To highlight this unique property of current photocatalysts, all of the photoreactions in this work were conducted under the visible part of the light (wavelength 400–700 nm). The optical band gap energy of the hematene and the Ru-hematene calculated by the Tauc plot [66] based on the Kubelka-Munk [67] theory was 1.70 and 1.71 eV, respectively (Fig. 6b). It should be noted that in spite of the huge difference in absorbed light, the band gap of the photocatalysts was almost the same.

As discussed in detail, the presence of RuO_2 was proved by the surface XPS analysis (Fig. 5a). This oxidation occurred probably during the calcination step at 300 °C. Nagaoka and coworkers [68] reported that RuO_2 produces a catalytic surface for exothermic adsorption of NH_3. This chemisorption of ammonia decreased the overall thermodynamic energy needed for its decomposition. Then, the subsequent photo absorption by hematene resulted in the generation of electrons and holes. The holes were able to oxidize the already absorbed NH_3 through the quasi-metallic ruthenium oxide and left the electrons in the hematene for the reduction of the ammonia.

The control experiments show that the catalytic activity of hematene and ruthenium loaded hematene for decomposition of ammonia under dark condition is almost zero. Furthermore, the photodecomposition of ammonia as ammonium hydroxide without the presence of photocatalyst at 24 °C is zero.

After the ruthenium oxide was confirmed as a proper co-catalyst for hematene to decompose the ammonia, the loading optimization of Ru was performed. Fig. 6c shows that loading the hematene with the optimum amount of Ru—0.5 wt. %—led to a continuously increased amount of H_2. In lower amounts of the Ru loading, the charge separation was not effective enough to produce hydrogen, while a higher amount of Ru was able to produce charge recombination centers at the surface of the hematene [68]. All the characterization was done while loading the hematene with 0.5 wt.% of Ru, labelled as Ru-hematene.

To have a fair and reliable comparison between the photoactivity of the hematene and the Ru-hematene, the mass of the photocatalyst had to be optimized against the photoactivity (Fig. 6d and Fig. S4). The reason is that the amount of the H_2 production during the photocatalytic reaction is not necessarily proportional to the mass of the photocatalyst due to the limitation of light absorption and diffusion conditions [69, 70]. It is obvious from Fig. 6d that the loading of 2 mg of the photocatalyst in both cases was able to produce the optimum amount of the product. This plot shows that the Ru-hematene photocatalyst produced 2.5 times more H_2 than the pristine hematene under optimum conditions.

The Ru-hematene showed an 11% decrease in activity after five photocatalytic runs for the total of 120 h (Fig. 6e). A constant decrease in activity after each run could be correlated to a loss in the photocatalyst caused by the attachment to the reactor walls and even to the magnet stirrer. Additionally, as the catalyst was not washed after each run of the photoreaction, the surface of the catalyst could have been passivated by reactants, products or intermediate species.

4. Conclusions

A non-van der Waals 2D material, hematene, was simply prepared via the exfoliation of iron oxide ore specularite, deploying an (ultra)pure water solution. Using this strategy, the prepared material exhibited favorable electrochemical properties in terms of charge transfer and diffusion limiting processes. As a proof-of-concept, we have amply demonstrated that this pure n-vdW material can be easily modified with ruthenium oxide nanoparticles and can serve as a catalytic eco-friendly platform for the photocatalytic decomposition of an aqueous solution of ammonia in order to produce hydrogen via the visible light irradiation. The obtained results proved that the combination of RuO_2 catalytic surface with the conductive 2D hematene substrate exhibited a synergic effect in terms of the generation of electrons and holes. Based on the results, the holes were able to oxidize the already absorbed ammonia through the quasi-metallic ruthenium oxide and left the electrons in the

hematene for the reduction of ammonia. Experimental data indicate that the optimum dosage of ruthenium was around 0.5 wt %, yielding the maximum amount of hydrogen after 24 hours. With respect to the pristine hematene, a co-doped material provided at least 2.5 times better photocatalytic response towards hydrogen evolution. Without any cleaning steps, the Ru-hematene photocatalyst exhibited only 11 % of the photocatalytic reaction decrease after five successful photocatalytic runs, predisposing it for practical application. The discovery opens up possibilities for creating robust and effective photocatalysts for a wide range of applications using non-van der Waals 2D materials and metal oxide nanoparticles.

CRediT authorship contribution statement

Jana Dzíbelová: Investigation, Writing – original draft, Writing – review & editing. **S.M. Hossein Hejazi:** Conceptualization, Investigation, Writing – original draft, Writing – review & editing. **Veronika Šedajová:** Investigation, Writing – original draft. **David Panáček:** Investigation, Writing – original draft. **Petr Jakubec:** Conceptualization, Writing – original draft, Writing – review & editing. **Zdeněk Baďura:** Investigation, Writing – original draft. **Ondřej Malina:** Investigation, Writing – original draft, Writing – review & editing. **Josef Kašlík:** Investigation. **Jan Filip:** Conceptualization. **Štěpán Kment:** Conceptualization. **Michal Otyepka:** Conceptualization, Writing – review & editing. **Radek Zbořil:** Conceptualization, Writing – original draft, Writing – review & editing.

Declaration of Competing Interest

The authors declare that they have no known competing financial interests or personal relationships that could have appeared to influence the work reported in this paper.

Data availability

Data will be made available on request.

Acknowledgments

R.Z. acknowledges the support from the Czech Science Foundation, project No. 19–27454X. P.J. acknowledges the Research Infrastructure NanoEnviCz, supported by the Ministry of Education, Youth and Sports of the Czech Republic under Project No. LM2018124. We also acknowledge the support from ERDF/ESF "Nano4Future" (No. CZ.02.1.01/0.0/0.0/16_019/0000754) and the Technology Agency of the Czech Republic, Program TREND (GEFSEM, FW01010183). The authors gratefully thank Ondřej Tomanec (HR-TEM); Jiří Hošek (CPEM); Kateřina Roháčová (Raman); and Jan Pauswang (part of electrochemical testing).

Supplementary materials

Supplementary material associated with this article can be found, in the online version, at doi:10.1016/j.apmt.2023.101881.

References

[1] A. Gupta, T. Sakthivel, S. Seal, Recent development in 2D materials beyond graphene, Prog. Mater. Sci. 73 (2015) 44–126, https://doi.org/10.1016/j.pmatsci.2015.02.002.
[2] Z. Lin, Y. Liu, U. Halim, M. Ding, Y. Liu, Y. Wang, C. Jia, P. Chen, X. Duan, C. Wang, F. Song, M. Li, C. Wan, Y. Huang, X. Duan, Solution-processable 2D semiconductors for high-performance large-area electronics, Nature 562 (2018) 254–258, https://doi.org/10.1038/s41586-018-0574-4.
[3] Q.A. Vu, Y.S. Shin, Y.R. Kim, V.L. Nguyen, W.T. Kang, H. Kim, D.H. Luong, I. M. Lee, K. Lee, D.S. Ko, J. Heo, S. Park, Y.H. Lee, W.J. Yu, Two-terminal floating-gate memory with van der Waals heterostructures for ultrahigh on/off ratio, Nat. Commun. 7 (2016) 12725, https://doi.org/10.1038/ncomms12725.
[4] S. Jiao, L. Liu, J. Wang, K. Ma, J. Lv, A novel biosensor based on molybdenum disulfide (MoS_2) modified porous anodic aluminum oxide nanochannels for ultrasensitive microRNA-155 detection, Small 16 (2020), 2001223, https://doi.org/10.1002/smll.202001223.
[5] X. Chen, Y.J. Park, M. Kang, S.K. Kang, J. Koo, S.M. Shinde, J. Shin, S. Jeon, G. Park, Y. Yan, M.R. MacEwan, W.Z. Ray, K.M. Lee, J.A. Rogers, J.H. Ahn, CVD-grown monolayer MoS_2 in bioabsorbable electronics and biosensors, Nat. Commun. 9 (2018) 1690, https://doi.org/10.1038/s41467-018-03956-9.
[6] T. Kaewmaraya, L. Ngamwongwan, P. Moontragoon, W. Jarernboon, D. Singh, R. Ahuja, A. Karton, T. Hussain, Novel green phosphorene as a superior chemical gas sensing material, J. Hazard. Mater. 401 (2021), 123340, https://doi.org/10.1016/j.jhazmat.2020.123340.
[7] D. Kundu, B.D. Adams, V. Duffort, S.H. Vajargah, L.F. Nazar, A high-capacity and long-life aqueous rechargeable zinc battery using a metal oxide intercalation cathode, Nat. Energy 1 (2016) 16119, https://doi.org/10.1038/nenergy.2016.119.
[8] M. Jana, R. Xu, X.B. Cheng, J.S. Yeon, J.M. Park, J.Q. Huang, Q. Zhang, H.S. Park, Rational design of two-dimensional nanomaterials for lithium–sulfur batteries, Energy Environ. Sci. 13 (2020) 1049–1075, https://doi.org/10.1039/C9EE02049G.
[9] A.S. Agnihotri, A. Varghese, N. M, Transition metal oxides in electrochemical and bio sensing: a state-of-art review, Appl. Surf. Sci. Adv. 4 (2021), 100072, https://doi.org/10.1016/j.apsadv.2021.100072.
[10] C. Gong, L. Li, Z. Li, H. Ji, A. Stern, Y. Xia, T. Cao, W. Bao, C. Wang, Y. Wang, Z. Q. Qiu, R.J. Cava, S.G. Louie, J. Xia, X. Zhang, Discovery of intrinsic ferromagnetism in two-dimensional van der Waals crystals, Nature 546 (2017) 265–269, https://doi.org/10.1038/nature22060.
[11] B. Huang, G. Clark, E. Navarro-Moratalla, D.R. Klein, R. Cheng, K.L. Seyler, D. Zhong, E. Schmidgall, M.A. McGuire, D.H. Cobden, W. Yao, D. Xiao, P. Jarillo-Herrero, X. Xu, Layer-dependent ferromagnetism in a van der Waals crystal down to the monolayer limit, Nature 546 (2017) 270–273, https://doi.org/10.1038/nature22391.
[12] H. Wang, J. Chen, Y. Lin, X. Wang, J. Li, Y. Li, L. Gao, L. Zhang, D. Chao, X. Xiao, J.-M. Lee, Electronic modulation of non-van der Waals 2D electrocatalysts for efficient energy conversion, Adv. Mater. 33 (2021), 2008422, https://doi.org/10.1002/adma.202008422.
[13] Y. Wang, Z. Zhang, Y. Mao, X. Wang, Two-dimensional nonlayered materials for electrocatalysis, Energy Environ. Sci. 13 (2020) 3993–4016, https://doi.org/10.1039/D0EE01714K.
[14] X. Huang, S. Tang, X. Mu, Y. Dai, G. Chen, Z. Zhou, F. Ruan, Z. Yang, N. Zheng, Freestanding palladium nanosheets with plasmonic and catalytic properties, Nat. Nanotechnol. 6 (2011) 28–32, https://doi.org/10.1038/nnano.2010.235.
[15] M. Luo, Z. Zhao, Y. Zhang, Y. Sun, Y. Xing, F. Lv, Y. Yang, X. Zhang, S. Hwang, Y. Qin, J.Y. Ma, F. Lin, D. Su, G. Lu, S. Guo, PdMo bimetallene for oxygen reduction catalysis, Nature 574 (2019) 81–85, https://doi.org/10.1038/s41586-019-1603-7.
[16] H. Duan, N. Yan, R. Yu, C.R. Chang, G. Zhou, H.S. Hu, H. Rong, Z. Niu, J. Mao, H. Asakura, T. Tanaka, P.J. Dyson, J. Li, Y. Li, Ultrathin rhodium nanosheets, Nat. Commun. 5 (2014) 3093, https://doi.org/10.1038/ncomms4093.
[17] A. Zavabeti, J.Z. Ou, B.J. Carey, N. Syed, R. Orrell-Trigg, E.L.H. Mayes, C. Xu, O. Kavehei, A.P. O'Mullane, R.B. Kaner, K. Kalantar-zadeh, T. Daeneke, A liquid metal reaction environment for the room-temperature synthesis of atomically thin metal oxides, Science 358 (2017) 332–335, https://doi.org/10.1126/science.aao4249.
[18] Y. Dou, J. Xu, B. Ruan, Q. Liu, Y. Pan, Z. Sun, S.X. Dou, Atomic layer-by-Layer Co_3O_4/graphene composite for high performance lithium-ion batteries, Adv. Energy Mater. 6 (2016), 1501835, https://doi.org/10.1002/aenm.201501835.
[19] S. Qamar, F. Lei, L. Liang, S. Gao, K. Liu, Y. Sun, W. Ni, Y. Xie, Ultrathin TiO_2 flakes optimizing solar light driven CO_2 reduction, Nano Energy 26 (2016) 692–698, https://doi.org/10.1016/j.nanoen.2016.06.029.
[20] J. Cao, T. Li, H. Gao, Y. Lin, X. Wang, H. Wang, T. Palacios, X. Ling, Realization of 2D crystalline metal nitrides via selective atomic substitution, Sci. Adv. 6 (2020) eaax8784, https://doi.org/10.1126/sciadv.aax8784.
[21] H. Wu, X. Lu, G. Zheng, G.W. Ho, Topotactic engineering of ultrathin 2D nonlayered nickel selenides for full water electrolysis, Adv. Energy Mater. 8 (2018), 1702704, https://doi.org/10.1002/aenm.201702704.
[22] C. Jin, L. Kou, Two-dimensional non-van der Waals magnetic layers: functional materials for potential device applications, J. Phys. Appl. Phys. 54 (2021), 413001, https://doi.org/10.1088/1361-6463/ac08ca.
[23] R. Ramírez-Jiménez, M. Franco, E. Rodrigo, R. Sainz, R. Ferritto, A.M. Lamsabhi, J. L. Aceña, M.B. Cid, Unexpected reactivity of graphene oxide with DBU and DMF, J. Mater. Chem. A 6 (2018) 12637–12646, https://doi.org/10.1039/C8TA03529F.
[24] J. Mráz, H. Cross, A. Gescher, M.D. Threadgill, J. Flek, Differences between rodents and humans in the metabolic toxification of N,N-dimethylformamide, Toxicol. Appl. Pharmacol. 98 (1989) 507–516, https://doi.org/10.1016/0041-008X(89)90179-8.
[25] G. Groth, K. Kronauer, K.J. Freundt, Effects of N,N-dimethylformamide and its degradation products in zebrafish embryos, Toxicol. *In Vitro* 8 (1994) 401–406, https://doi.org/10.1016/0887-2333(94)90161-9.
[26] Commission Regulation (EU) 2021/2030 of 19 November 2021 amending Annex XVII to Regulation (EC) No 1907/2006 of the European Parliament and of the Council concerning the Registration, Evaluation, Authorisation and Restriction of Chemicals (REACH) as regards N,N-dimethylformamide (Text with EEA relevance). Document 32021R2030. https://eur-lex.europa.eu/legal-content/EN/TXT/PDF/?uri=CELEX:32021R2030&from=EN.

[27] N.S. Lewis, D.G. Nocera, Powering the planet: chemical challenges in solar energy utilization, Proc. Natl. Acad. Sci. 103 (2006) 15729–15735, https://doi.org/10.1073/pnas.0603395103.

[28] A. Puthirath Balan, S. Radhakrishnan, C.F. Woellner, S.K. Sinha, L. Deng, C. de los Reyes, B.M. Rao, M. Paulose, R. Neupane, A. Apte, V. Kochat, R. Vajtai, A. R. Harutyunyan, C.W. Chu, G. Costin, D.S. Galvao, A.A. Martí, P.A. van Aken, O. K. Varghese, C.S. Tiwary, A. Malie Madom Ramaswamy Iyer, P.M. Ajayan, Exfoliation of a non-van der Waals material from iron ore hematite, Nat. Nanotechnol. 13 (2018) 602–609, https://doi.org/10.1038/s41565-018-0134-y.

[29] A. Puthirath Balan, S. Radhakrishnan, R. Kumar, R. Neupane, S.K. Sinha, L. Deng, C.A. Reyes, A. Apte, B.M. Rao, M. Paulose, R. Vajtai, C.W. Chu, G. Costin, A. A. Martí, O.K. Varghese, A.K. Singh, C.S. Tiwary, M.R. Anantharaman, P. M. Ajayan, A non-van der Waals two-dimensional material from natural titanium mineral ore Ilmenite, Chem. Mater. 30 (2018) 5923–5931, https://doi.org/10.1021/acs.chemmater.8b01935.

[30] F. Schüth, R. Palkovits, R. Schlögl, D.S. Su, Ammonia as a possible element in an energy infrastructure: catalysts for ammonia decomposition, Energy Environ. Sci. 5 (2012) 6278–6289, https://doi.org/10.1039/C2EE02865D.

[31] S. Zhang, Z. He, X. Li, J. Zhang, Q. Zang, S. Wang, Building heterogeneous nanostructures for photocatalytic ammonia decomposition, Nanoscale. Adv. 2 (2020) 3610–3623, https://doi.org/10.1039/D0NA00161A.

[32] W.I.F. David, J.W. Makepeace, S.K. Callear, H.M.A. Hunter, J.D. Taylor, T.J. Wood, M.O. Jones, Hydrogen production from ammonia using sodium amide, J. Am. Chem. Soc. 136 (2014) 13082–13085, https://doi.org/10.1021/ja5042836.

[33] A. Iwase, K. Ii, A. Kudo, Decomposition of an aqueous ammonia solution as a photon energy conversion reaction using a Ru-loaded ZnS photocatalyst, Chem. Commun. 54 (2018) 6117–6119, https://doi.org/10.1039/C8CC02639D.

[34] A. Utsunomiya, A. Okemoto, Y. Nishino, K. Kitagawa, H. Kobayashi, K. Taniya, Y. Ichihashi, S. Nishiyama, Mechanistic study of reaction mechanism on ammonia photodecomposition over Ni/TiO_2 photocatalysts, Appl. Catal. B Environ. 206 (2017) 378–383, https://doi.org/10.1016/j.apcatb.2017.01.045.

[35] K. Obata, K. Kishishita, A. Okemoto, K. Taniya, Y. Ichihashi, S. Nishiyama, Photocatalytic decomposition of NH_3 over TiO_2 catalysts doped with Fe, Appl. Catal. B Environ. 160–161 (2014) 200–203, https://doi.org/10.1016/j.apcatb.2014.05.033.

[36] E. Bahadori, F. Conte, A. Tripodi, G. Ramis, I. Rossetti, Photocatalytic selective oxidation of ammonia in a semi-batch reactor: unravelling the effect of reaction conditions and metal co-catalysts, Catalysts 11 (2021) 209, https://doi.org/10.3390/catal11020209.

[37] H. Yuzawa, T. Mori, H. Itoh, H. Yoshida, Reaction mechanism of ammonia decomposition to nitrogen and hydrogen over metal loaded titanium oxide photocatalyst, J. Phys. Chem. C 116 (2012) 4126–4136, https://doi.org/10.1021/jp209795t.

[38] Y. Shu, J. Ji, M. Zhou, S. Liang, Q. Xie, S. Li, B. Liu, J. Deng, J. Cao, S. Liu, H. Huang, Selective photocatalytic oxidation of gaseous ammonia at ppb level over Pt and F modified TiO_2, Appl. Catal. B Environ. 300 (2022), 120688, https://doi.org/10.1016/j.apcatb.2021.120688.

[39] M. Reli, M. Edelmannová, M. Šihor, P. Praus, L. Svoboda, K.K. Mamulová, H. Otoupalíková, L. Čapek, A. Hospodková, L. Obalová, K. Kočí, Photocatalytic H_2 generation from aqueous ammonia solution using ZnO photocatalysts prepared by different methods, Int. J. Hydrog. Energy. 40 (2015) 8530–8538, https://doi.org/10.1016/j.ijhydene.2015.05.004.

[40] Z. Mohammadi, S. Sharifnia, Y. Shavisi, Photocatalytic degradation of aqueous ammonia by using TiO2ZnO/LECA hybrid photocatalyst, Mater. Chem. Phys. 184 (2016) 110–117, https://doi.org/10.1016/j.matchemphys.2016.09.031.

[41] H. Wang, Y. Su, H. Zhao, H. Yu, S. Chen, Y. Zhang, X. Quan, Photocatalytic oxidation of aqueous ammonia using atomic single layer graphitic-C_3N_4, Environ. Sci. Technol. 48 (2014) 11984–11990, https://doi.org/10.1021/es503073z.

[42] R. Wang, T. Xie, Z. Sun, T. Pu, W. Li, J.P. Ao, Graphene quantum dot modified g-C_3N_4 for enhanced photocatalytic oxidation of ammonia performance, RSC Adv. 7 (2017) 51687–51694, https://doi.org/10.1039/C7RA07988E.

[43] H. Xu, B.W. Zeiger, K.S. Suslick, Sonochemical synthesis of nanomaterials, Chem. Soc. Rev. 42 (2013) 2555–2567, https://doi.org/10.1039/C2CS35282F.

[44] T. Fujii, F.M.F. de Groot, G.A. Sawatzky, F.C. Voogt, T. Hibma, K. Okada, In situ XPS analysis of various iron oxide films grown by NO_2-assisted molecular-beam epitaxy, Phys. Rev. B 59 (1999) 3195–3202, https://doi.org/10.1103/PhysRevB.59.3195.

[45] R.P. Gupta, S.K. Sen, Calculation of multiplet structure of core p -vacancy levels. II, Phys. Rev. B 12 (1975) 15–19, https://doi.org/10.1103/PhysRevB.12.15.

[46] M.C. Biesinger, B.P. Payne, A.P. Grosvenor, L.W.M. Lau, A.R. Gerson, R.S.C. Smart, Resolving surface chemical states in XPS analysis of first row transition metals, oxides and hydroxides: Cr, Mn, Fe, Co and Ni, Appl. Surf. Sci. 257 (2011) 2717–2730, https://doi.org/10.1016/j.apsusc.2010.10.051.

[47] X. Lu, Y. Zeng, M. Yu, T. Zhai, C. Liang, S. Xie, M.-S. Balogun, Y. Tong, Oxygen-deficient hematite nanorods as high-performance and novel negative electrodes for flexible asymmetric supercapacitors, Adv. Mater. 26 (2014) 3148–3155, https://doi.org/10.1002/adma.201305851.

[48] S. Chahal, S.M. Kauzlarich, P. Kumar, Microwave synthesis of hematene and other two-dimensional oxides, ACS Mater. Lett. 3 (2021) 631–640, https://doi.org/10.1021/acsmaterialslett.1c00102.

[49] D.L.A. de Faria, S. Venâncio Silva, M.T. de Oliveira, Raman microspectroscopy of some iron oxides and oxyhydroxides, J. Raman Spectrosc. 28 (1997) 873–878, https://doi.org/10.1002/(SICI)1097-4555(199711)28:11<873::AID-JRS177>3.0.CO;2-B.

[50] A. Thejas Prasannakumar, B. C, R. R, R.F. U, R. Philip, S.J Varma, Hematene nanoflakes: a non-van der Waals material with superior nonlinear optical properties, ACS Appl. Opt. Mater. (2022), https://doi.org/10.1021/acsaom.2c00071.

[51] S.-H. Shim, T.S. Duffy, Raman spectroscopy of Fe_2O_3 to 62GPa, Am. Mineral. 87 (2002) 318–326, https://doi.org/10.2138/am-2002-2-314.

[52] Z. Zhang, M. Ye, E.J. Harvey, G. Merle, Editors' choice—methanol electrooxidation with platinum decorated hematene nanosheet, J. Electrochem. Soc. 166 (2019) H135, https://doi.org/10.1149/2.0661904jes.

[53] U. Holzwarth, N. Gibson, The Scherrer equation versus the "Debye-Scherrer equation, Nat. Nanotechnol. 6 (2011) 534, https://doi.org/10.1038/nnano.2011.145.

[54] B.-Y. Chang, S.-M. Park, Electrochemical impedance spectroscopy, Annu. Rev. Anal. Chem. 3 (2010) 207–229, https://doi.org/10.1146/annurev.anchem.012809.102211.

[55] A.R.C. Bredar, A.L. Chown, A.R. Burton, B.H. Farnum, Electrochemical impedance spectroscopy of metal oxide electrodes for energy applications, ACS Appl. Energy Mater. 3 (2020) 66–98, https://doi.org/10.1021/acsaem.9b01965.

[56] D.J. Morgan, Resolving ruthenium: XPS studies of common ruthenium materials, Surf. Interface Anal. 47 (2015) 1072–1079, https://doi.org/10.1002/sia.5852.

[57] J.Y. Shen, A. Adnot, S. Kaliaguine, An ESCA study of the interaction of oxygen with the surface of ruthenium, Appl. Surf. Sci. 51 (1991) 47–60, https://doi.org/10.1016/0169-4332(91)90061-N.

[58] S. Hao, M. Liu, J. Pan, X. Liu, X. Tan, N. Xu, Y. He, L. Lei, X. Zhang, Dopants fixation of Ruthenium for boosting acidic oxygen evolution stability and activity, Nat. Commun. 11 (2020) 5368, https://doi.org/10.1038/s41467-020-19212-y.

[59] S. Cattaneo, H. Naslhajian, F. Somodi, C. Evangelisti, A. Villa, L. Prati, Ruthenium on carbonaceous materials for the selective hydrogenation of HMF, Molecules 23 (2018) 2007, https://doi.org/10.3390/molecules23082007.

[60] R. Bavand, A. Yelon, E. Sacher, X-ray photoelectron spectroscopic and morphologic studies of Ru nanoparticles deposited onto highly oriented pyrolytic graphite, Appl. Surf. Sci. 355 (2015) 279–289, https://doi.org/10.1016/j.apsusc.2015.06.202.

[61] N. Chakroune, G. Viau, S. Ammar, L. Poul, D. Veautier, M.M. Chehimi, C. Mangeney, F. Villain, F. Fiévet, Acetate- and Thiol-Capped Monodisperse Ruthenium Nanoparticles: XPS, XAS, and HRTEM Studies, Langmuir 21 (2005) 6788–6796, https://doi.org/10.1021/la050706c.

[62] Q. Liu, B. Lu, F. Nichols, J. Ko, R. Mercado, F. Bridges, S. Chen, Rapid preparation of carbon-supported ruthenium nanoparticles by magnetic induction heating for efficient hydrogen evolution reaction in both acidic and alkaline media, SusMat 2 (2022) 335–346, https://doi.org/10.1002/sus2.66.

[63] S.M.H. Hejazi, M. Shahrezaei, P. Błoński, M. Allieta, P.M. Sheverdyaeva, P. Moras, Z. Baďura, S. Kalytchuk, E. Mohammadi, R. Zbořil, Š. Kment, M. Otyepka, A. Naldoni, P. Fornasiero, Defect engineering over anisotropic brookite toward substrate-specific photo-oxidation of alcohols, Chem. Catal. 2 (2022) 1177–1190, https://doi.org/10.1016/j.checat.2022.03.015.

[64] Y. Gao, J.K. Kuncheria, H.A. Jenkins, R.J. Puddephatt, G.P.A. Yap, The interconversion of formic acid and hydrogen/carbon dioxide using a binuclear ruthenium complex catalyst, J. Chem. Soc. Dalton Trans. (2000) 3212–3217, https://doi.org/10.1039/b004234j.

[65] M. Lin, L.X. Dai, J. Gu, L.Q. Kang, Y.H. Wang, R. Si, Z.Q. Zhao, W.C. Liu, X. Fu, L. D. Sun, Y.W. Zhang, C.H. Yan, Moderate oxidation levels of Ru nanoparticles enhance molecular oxygen activation for cross-dehydrogenative-coupling reactions via single electron transfer, RSC Adv. 7 (2017) 33078–33085, https://doi.org/10.1039/C7RA05726A.

[66] J. Tauc, R. Grigorovici, V. Vancu, Optical properties and electronic structure of amorphous germanium, Phys. Stat. Sol. 15 (1966) 627–637.

[67] P. Makuła, M. Pacia, W. Macyk, How to correctly determine the band gap energy of modified semiconductor photocatalysts based on UV–Vis spectra, J. Phys. Chem. Lett. 9 (2018) 6814–6817, https://doi.org/10.1021/acs.jpclett.8b02892.

[68] K. Nagaoka, T. Eboshi, Y. Takeishi, R. Tasaki, K. Honda, K. Imamura, K. Sato, Carbon-free H_2 production from ammonia triggered at room temperature with an acidic RuO_2/γ-Al_2O_3 catalyst, Sci. Adv. 3 (2017), e1602747, https://doi.org/10.1126/sciadv.1602747.

[69] S. Cao, L. Piao, Considerations for a more accurate evaluation method for photocatalytic water splitting, Angew. Chem. 132 (2020) 18468–18476, https://doi.org/10.1002/ange.202009633.

[70] M. Qureshi, K. Takanabe, Insights on measuring and reporting heterogeneous photocatalysis: efficiency definitions and setup examples, Chem. Mater. 29 (2017) 158–167, https://doi.org/10.1021/acs.chemmater.6b02907.